CrossMark

Spatially Resolved Modeling of Optical Albedos for a Sample of Six Hot Jupiters

Danica J. Adams[1] , Tiffany Kataria[2] , Natasha E. Batalha[3] , Peter Gao[4,5] , and Heather A. Knutson[1]

[1] Division of Geological and Planetary Sciences, California Institute of Technology, Pasadena, CA 91125, USA; djadams@caltech.edu
[2] Jet Propulsion Laboratory, California Institute of Technology, Pasadena, CA 91109, USA
[3] NASA Ames Research Center, MS 245-3, Moffett Field, CA 94035, USA
[4] Department of Astronomy and Astrophysics, University of California, Santa Cruz, Santa Cruz, CA 95064, USA
[5] Earth and Planets Laboratory, Carnegie Institution for Science, 5241 Broad Branch Road, NW, Washington, DC 20015, USA

Abstract

Optical secondary eclipse measurements made by Kepler reveal a diverse set of geometric albedos for hot Jupiters with equilibrium temperatures between 1550 and 1700 K. The presence or absence of high-altitude condensates, such as Mg_2SiO_4, Fe, Al_2O_3, and TiO_2, can significantly alter optical albedos, but these clouds are expected to be confined to localized regions in the atmospheres of these tidally locked planets. Here, we present 3D general circulation models and corresponding cloud and albedo maps for six hot Jupiters with measured optical albedos in this temperature range. We find that the observed optical albedos of K2-31b and K2-107b are best matched by either cloud-free models or models with relatively compact cloud layers, while Kepler-8b's and Kepler-17b's optical albedos can be matched by moderately extended ($f_{sed} = 0.1$) parametric cloud models. HATS-11b has a high optical albedo, corresponding to models with bright Mg_2SiO_4 clouds extending to very low pressures ($f_{sed} = 0.03$). We are unable to reproduce Kepler-7b's high albedo, as our models predict that the dayside will be dominated by dark Al_2O_3 clouds at most longitudes. We compare our parametric cloud model with a microphysical cloud model. We find that even after accounting for the 3D thermal structure, no single cloud model can explain the full range of observed albedos within the sample. We conclude that a better knowledge of the vertical mixing profiles, cloud radiative feedback, cloud condensate properties, and atmospheric metallicities is needed in order to explain the unexpected diversity of albedos in this temperature range.

Unified Astronomy Thesaurus concepts: Hot Jupiters (753); Atmospheric clouds (2180); Radiative transfer (1335); Exoplanet atmospheres (487); Extrasolar gaseous planets (2172)

1. Introduction

Transiting short-period gas giant planets, or "hot Jupiters", are among the most favorable targets for atmospheric characterization studies. By observing the decrease in optical flux when the planet passes behind the host star (secondary eclipse), we can measure the optical dayside albedos for these tidally locked planets. Most of these albedo measurements have come from space telescopes observing in broad optical bandpasses (e.g., Rowe et al. 2008; Demory et al. 2011; Kipping & Bakos 2011; Coughlin & Lopez-Morales 2012; Demory et al. 2013; Parviainen et al. 2013; Angerhausen et al. 2014; von Paris et al. 2016; Niraula et al. 2018). The hot Jupiter HD 189733b is currently the only planet with a spectroscopically resolved reflected-light measurement (Evans et al. 2013; geometric albedo of 0.40 ± 0.12 at 290–450 nm and <0.12 at 450–570 nm). WASP-12b and WASP-43b were also observed with optical spectrographs on the Hubble Space Telescope (HST), but both observations resulted in nondetections (Bell et al. 2017; Fraine et al. 2021; geometric albedos <0.06). These spectroscopic albedo measurements are invaluable for constraining the nature of the scattering particles in the atmospheres of these planets (e.g., Barstow et al. 2014).

Theoretical models predict that variations in hot Jupiter optical albedos should primarily be driven by the presence or absence of high-altitude aerosols, which are expected to scatter incident starlight (e.g., Seager et al. 2000; Burrows et al. 2008). Cloud-free

atmosphere models for hot Jupiters generally predict dayside albedos of less than 0.1 (Seager et al. 2000), but the observed optical geometric albedo measurements published to date span a wide range of values, with the brightest planets exhibiting albedos as high as 0.3 (e.g., Heng & Demory 2013; Niraula et al. 2018). In the solar system, the presence of water clouds increases Earth's geometric albedo to approximately 0.37 (e.g., Goode et al. 2001), while ammonia clouds in Jupiter's atmosphere contribute to its geometric albedo of approximately 0.5 (e.g., Marley et al. 1999). For the same reason, models suggest that the presence of reflective condensates such as Mg_2SiO_4 or $MgSiO_3$ in hot Jupiter atmospheres can increase their albedos to values as high as 0.5 (Parmentier et al. 2016, 2021; Roman et al. 2021). Unlike brown dwarfs, whose cloud distributions and optical depths correlate closely with their equilibrium temperatures (e.g., Kirkpatrick 2005; Marley et al. 2010), hot Jupiter albedos can vary by as much as an order of magnitude within a relatively narrow range of equilibrium temperatures (Figure 1). This suggests that individual planets with similar equilibrium temperatures may exhibit diverse cloud properties.

Hot Jupiters are expected to be tidally locked as a result of their short orbital periods, which can lead to significant day–night temperature gradients (e.g., Guillot & Showman 2002). This inhomogeneous temperature structure affects the cloud distribution, and 3D atmospheric circulation models predict that hot Jupiters should host spatially inhomogeneous clouds over a wide range of equilibrium temperatures (e.g., Parmentier et al. 2016, 2021; Roman et al. 2021; also see Figure 1). Furthermore, there is direct observational evidence for inhomogeneous cloud structures stemming from reflected-light phase curves (e.g.,
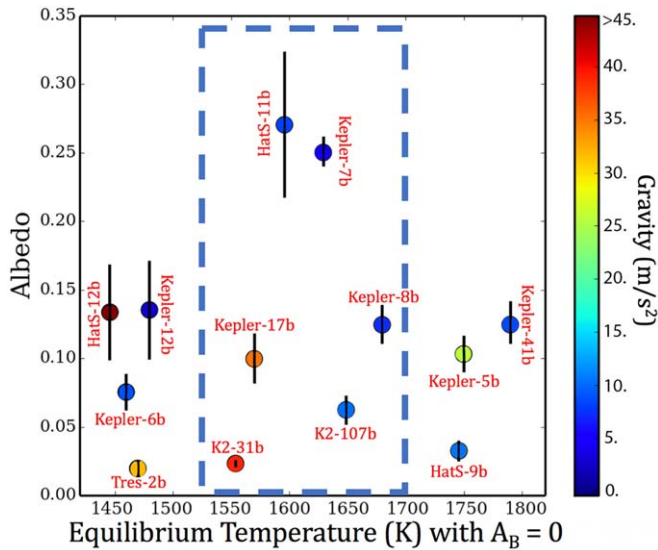
Figure 1. Optical geometric albedo measurements for a sample of hot Jupiters observed in the Kepler bandpass; at these temperatures thermal emission is negligible for planets with cloudy skies and the measured secondary eclipse depth is dominated by reflected light. The equilibrium temperature is calculated assuming a Bond albedo of zero and efficient day–night circulation. The planet colors vary as a function of surface gravity. The dashed box indicates the temperature range considered in this study. Measurements are drawn from Fortney et al. (2011), Desert et al. (2011), Barclay et al. (2012), Esteves et al. (2013), Shporer & Hu (2015), Niraula et al. (2018), and Heng et al. (2021).

Demory et al. 2013). To date, three of the four planets with observed reflected-light phase curves appear to have patchy clouds (Desert et al. 2011; Demory et al. 2013; Angerhausen et al. 2014; Esteves et al. 2015; Shporer & Hu 2015; von Paris et al. 2016; Niraula et al. 2018). Kepler-7b, -12b, and -41b all appear to have patchy clouds that are preferentially concentrated in the western (dawn) hemisphere, causing the peak of the phase curve to occur after the secondary eclipse (Shporer & Hu 2015). Observations of the fourth planet, TrES-2b, indicate that it is uniformly dark ($A_s < 0.03$, which is equivalent to $A_g < 0.02$ for a Lambertian sphere, where A_s is the spherical albedo and A_g is the geometric albedo) at all phases (von Paris et al. 2016). These studies demonstrate that if we wish to explain the observed planet-to-planet variations in the measured dayside optical albedos of hot Jupiters, we must utilize 3D models capable of capturing the spatially varying cloud structure.

While an increasing number of studies are using general circulation models (GCMs) to predict cloud patterns, these have either focused on individual planets (e.g., Lee et al. 2015; Webber et al. 2015; Oreshenko et al. 2016; Lines et al. 2018; Helling 2019; Helling et al. 2019; Lines et al. 2019; Roman & Rauscher 2019; Helling et al. 2020) or generic grids of models (e.g., Parmentier et al. 2016, 2021; Roman et al. 2021). Of these listed studies, only five (Webber et al. 2015; Oreshenko et al. 2016; Parmentier et al. 2016, 2021; Roman et al. 2021) use their models to calculate predicted albedos in the Kepler bandpass. The question of why individual planets with similar equilibrium temperatures would exhibit widely varying cloud properties therefore remains largely unexplored in the literature.

Modeling the 3D structure of clouds can be computationally demanding, especially given the large number of parameters that must be considered (including but not limited to the particle number density and size distribution, spatial extent of the clouds, location of the cloud decks, number and composition of cloud species, and coupled radiative feedback). In examining the body

of published studies that use GCMs to predict hot Jupiter dayside albedos, we find that all of these studies make simplifying assumptions in order to conserve run time and numerical complexity. Oreshenko et al. (2016), for example, determined the locations of clouds by comparing the 3D thermal structure from a GCM with relevant condensation curves, but assumed a fixed particle size and local condensation only (i.e., they neglected vertical mixing) for the cloud layers. In Parmentier et al. (2016), cloud distributions were determined using the completed temperature structure calculated by a nongray cloud-free GCM, with a cloud-top minimum pressure fixed at 1 microbar. In Parmentier et al. (2021), cloud layers were also calculated using the thermal structure output from a GCM, but the prescribed vertical extent is limited by temperatures within the extent of 200 mbar to 1 μbar. Roman & Rauscher (2019) and Roman et al. (2021) differ significantly from the Parmentier models. In the former, cloud distributions were determined at each timestep in a double-gray GCM which included radiative feedback. They included extended clouds, which form when the temperature-pressure profile permits but are forced to taper off at pressures between 0.3 and 0.057 mbar. They also consider compact cases with varied optical thickness where the clouds are truncated and tapered off after approximately one scale height regardless of where their base forms. In Roman et al. (2021), they also consider a more extensive grid of planet models, while also varying cloud compositions, densities, and vertical extents. All of the studies listed above assumed homogeneous condensation, allowing them to treat each individual cloud species separately. Although there are studies in the literature that have combined GCMs with microphysical cloud models (e.g., Lee et al. 2015; Lines et al. 2018; Helling 2019; Helling et al. 2019, 2020), these models focused on individual planets and were limited in their albedo predictions in the Kepler bandpass. Although there are studies in the literature that have combined GCMs with microphysical cloud models (e.g., Lee et al. 2015; Lines et al. 2018; Helling 2019; Helling et al. 2019, 2020), these models focused on individual planets and were limited in their albedo predictions in the Kepler bandpass.

In this study, we utilize a suite of models to investigate the role of patchy clouds over a sample of six individual hot Jupiters, chosen due to their diverse observed albedos over a narrow range of equilibrium temperatures. In Section 2, we describe our sample selection and summarize our modeling approach. We use 3D GCMs to derive the thermal structures and eddy diffusion coefficients (K_{zz}). We then use Virga, a phase equilibrium cloud code, to make detailed maps of cloud structure over the dayside of each planet. We use Planetary Intensity Code for Atmospheric Scattering Observations (PICASO), a radiative transfer program, to calculate the corresponding geometric albedo maps and hemisphere-integrated dayside albedos. We also consider a microphysical code, Community Aerosol and Radiation Model for Atmospheres (CARMA), which enables us to take a closer look at the role of nucleation, condensation, and sedimentation in shaping the distribution of dayside clouds. In Section 3 we compare our predicted dayside-integrated optical albedos with observations of the six planets of interest. We then investigate the relative importance of various model assumptions, such as equilibrium condensation versus kinetic condensation, by comparing the Virga results with the CARMA results. Finally, we discuss the implications of our results in Section 4 and present our conclusions in Section 5.

Table 1
Properties of our Planet Sample

Planet	M_P (M_J)	R_P (R_J)	T_{eq}(K)[a]	g ($m\,s^{-2}$)	a (au)	Period (days)	Measured A_g	Reference[b]
K2-31b	1.77	1.06	1550	39.07	0.022	1.26	0.023 ± 0.002	1,**9**
Kepler-17b	2.45	1.31	1570	35.41	0.026	1.49	0.099 ± 0.017	2,**3**
HATS-11b	0.85	1.51	1560	7.97	0.051	3.62	0.270 ± 0.052	4,5,**9**
Kepler-7b	0.45	1.65	1630	4.16	0.062	4.89	0.25 ± 0.01	6,**8**
K2-107b	0.84	1.44	1650	10.26	0.048	3.31	0.062 ± 0.010	5,7,**9**
Kepler-8b	0.60	1.41	1680	7.32	0.047	3.85	0.124 ± 0.013	6,**10**

Notes. (1) Grziwa et al. (2016), (2) Desert et al. (2011), (3) Bonomo et al. (2017), (4) Bayliss et al. (2018), (5) Livingston et al. (2018), (6) Esteves et al. (2015), (7) Eigmuller et al. (2017), (8) Heng et al. (2021), (9) Niraula et al. (2018), (10) Esteves et al. (2013).
[a] Calculated assuming a Bond albedo of zero and efficient day–night recirculation.
[b] Reference to geometric albedo measurement is bolded for each row.

2. Methods

2.1. Planet Sample

In this study we focus on planets with equilibrium temperatures (T_{eq}, calculated assuming an albedo of zero and efficient day–night recirculation) between 1550 and 1700 K. For planets in this relatively narrow temperature range, we expect that reflective silicate clouds should dominate the optical dayside albedos (e.g., Parmentier et al. 2016; Powell et al. 2018; Gao et al. 2020; Parmentier et al. 2021; Roman et al. 2021). This temperature range contains some of the most reflective hot Jupiters observed to date, including Kepler-7b (Demory et al. 2013; Heng et al. 2021) and HATS-11b (Niraula et al. 2018). Note that two observed geometric albedos have been reported for Kepler-7b, and from here on we consider the most recent value from Heng et al. (2021). It also includes three moderately reflective hot Jupiters (Kepler-8b, Kepler-17b, and K2-107b; Desert et al. 2011; Esteves et al. 2013; Niraula et al. 2018) and one very dark hot Jupiter (K2-31b; Niraula et al. 2018). Previous studies (e.g., Demory et al. 2013) have concluded that planets with these equilibrium temperatures should have negligible amounts of thermal emission in the Kepler bandpass. We checked this by using PICASO to compute the predicted thermal emission for each of the six planets in our sample and found a contribution of 2 ppm or less. This is significantly smaller than the uncertainties on the secondary eclipse depths used to calculate the geometric albedos for these planets. Hence, throughout this paper we ignore the thermal contribution to the measured secondary eclipse depth in the Kepler bandpass.

In this study we present a GCM tailored to each of the six individual planets, which we use to predict planet-to-planet variations in cloud coverage and dayside albedo in the optical Kepler band. These planets sample a range of surface gravities, allowing us to investigate its effect on the planet's thermal structure, cloud distributions, and optical albedo. We summarize the physical and orbital properties of each system in Table 1.

2.2. Modeling Atmospheric Circulation with the SPARC/MITgcm

We model each planet's clear-sky (cloud-free) 3D thermal structure and atmospheric circulation with the Substellar and Planetary Radiation and Circulation (SPARC) model, which couples the GCM maintained at the Massachusetts Institute of Technology (the MITgcm; Adcrot et al. 2004) with a plane-parallel, two-stream version of the multistream radiation code, as described in Marley et al. (1999). The MITgcm solves the 3D primitive equations on a staggered Arakawa C grid (Arakawa et al. 1977) with the finite-volume method. The equations are discretized on a 128×64 cubed-sphere grid with 53 vertical layers extending from 200 bars at the bottom boundary to 20 μbar at the top boundary. A horizontal fourth-order Shapiro filter is used to smooth horizontal noise. We let each model run for a simulated 1000+ Earth days so as to reach quasi-steady-state equilibrium.

The radiative transfer scheme solves the two-stream radiative transfer equations using the correlated-k method (Goody et al. 1989; Marley et al. 1999) over 11 spectral bins (Kataria et al. 2013). This coupling allows for the self-consistent calculation of the heating and cooling rates of the atmosphere with latitude, longitude, and pressure. At each grid point, the radiative transfer scheme calculates the upward and downward fluxes at each pressure layer, which are used to update the heating/cooling rates. These rates are used by the MITgcm to update the wind and temperature fields. Opacities are computed at each pressure-temperature point assuming chemical and thermodynamic equilibrium, using the solar photospheric elemental abundances of Lodders (2003). We interpolate across the PHOENIX stellar atmosphere models to generate an input spectrum for each host star. The SPARC/MITgcm has been successfully utilized for a series of hot Jupiter studies (e.g., Showman et al. 2009; Kataria et al. 2013; Parmentier et al. 2013; Showman & Kaspi 2013; Lewis et al. 2014; Kataria et al. 2015; Showman et al. 2015; Kataria et al. 2016), and we refer the reader to Kataria et al. (2016) for further details. Figure 2 shows the resulting thermal structure for each of the six planets in our sample at 1 mbar (approximately the level of unit optical depth for clear skies).

2.3. Computing Equilibrium Condensate Clouds with Virga

We use the thermal structure and vertical mixing rates from the SPARC/MITgcm model as inputs to Virga (Batalha 2020),[6] an open-source code that calculates phase equilibrium cloud distributions. The cloud parameterization used in this code is described in Ackerman & Marley (2001) and has been used for 1D model studies across a wide range of exoplanets and brown dwarfs (e.g., Fortney et al. 2006; Marley et al. 2010; Morley et al. 2015). This parametric approach also allows us to sample the 3D cloud structure at a much higher spatial resolution than for our microphysical models.

We calculate K_{zz} profiles from the rms vertical velocities derived from global horizontal averages at a given pressure

---

[6] Code and documentation available at https://natashabatalha.github.io/virga/.
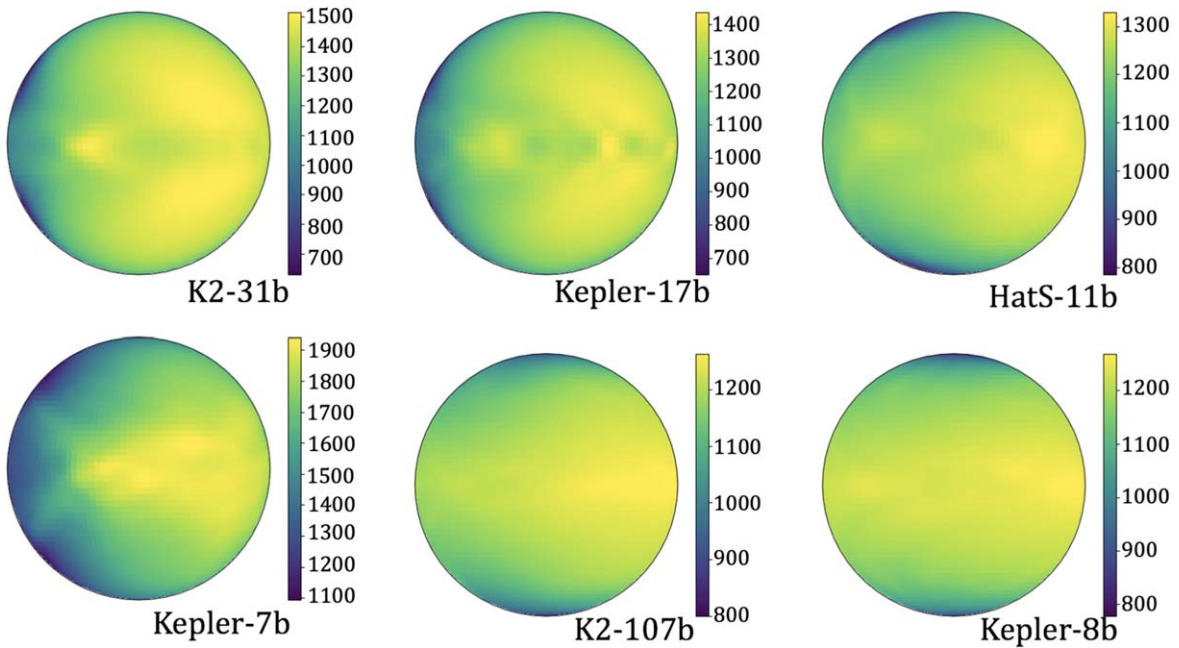
Figure 2. Map of the dayside temperatures (in Kelvin) of each planet at 1 mbar, roughly the pressure of unit optical depth in a clear atmosphere in the Kepler bandpass. Each planet is given a unique scale for the color bar to best match the relevant temperature range.

level from the GCMs by assuming $K_{zz} = w(z)L(z)$, where $w(z)$ is the horizontally averaged global rms vertical velocity from the GCM simulations, $L(z)$ is approximated as the atmospheric pressure scale height $H(z)$ (but could be a fraction of $H(z)$; see Smith 1998), and z is altitude. Moses et al. (2011) note that this is only an estimate; a better approach would involve calculating K_{zz} from the eddy vertical velocity times the eddy displacement, but this information is not readily obtainable from the GCMs; this could be resolved by adding passive tracers to future GCM models. Our treatment may overestimate K_{zz} in the $\sim$10–200 bar radiative region, where the vertical motion often consists of small-scale wave oscillations.

We reduce the spatial resolution of our longitude and latitude grid from 128×65 to 10×10 by binning the pressure-temperature profiles and corresponding K_{zz} profiles prior to running Virga. We retain the original 53 pressure levels in the rebinned grid. This binning has a negligible effect on our calculation of the phase-integrated albedo and significantly reduces computation time. We bin using the area mean with angles from the Chebyshev–Gauss integration method that vary as a function of planetary latitude and longitude.

In Virga the molar mixing ratio of the condensed phase, q_c, is calculated by solving the equation

$$-K_{zz}\frac{\partial q_t}{\partial z} - f_{\text{sed}}\,\omega_* q_c = 0, \qquad (1)$$

where q_t is the total mixing ratio (condensed and vapor phases), ω_* is the convective velocity scale, and f_{sed} is defined as the ratio of the mass-weighted droplet sedimentation velocity to the convective velocity, ω_*. The product $f_{\text{sed}}\omega_*$ describes an average sedimentation velocity for the condensate, which offsets turbulent mixing. We refer the reader to Ackerman & Marley (2001) for more details regarding the equations that govern Virga.

In Equation (1), f_{sed} is the only parameter that cannot be calculated directly from the models. We therefore treat it as a

tunable parameter and explore a range of possible values. Models with larger values of f_{sed} will have high rates of sedimentation, concentrating the condensing species in the lower atmosphere. Conversely, models with smaller values of f_{sed} will have much slower sedimentation rates, allowing cloud particles to remain lofted higher in the atmosphere. For each planet, we run a suite of Virga models with f_{sed} values of 0.03, 0.1, 0.3, 1.0, 3.0, and 6.0. This range is motivated by comparisons to observational data, which suggest that f_{sed} can be as small as 0.01 for super-Earths (Morley et al. 2015) or as large as 2–5 for some gas giants and brown dwarfs (Saumon & Marley 2008; Skemer et al. 2016; MacDonald et al. 2018). For Jupiter's ammonia clouds, an f_{sed} of $\sim$2 appears to provide the best match to observations (Ackerman & Marley 2001). We therefore conclude that our chosen list of values spans a representative range for this parameter.

2.4. Computing Microphysical Clouds with CARMA

In addition to the parametric model described above, we also utilize CARMA, a more computationally demanding microphysical cloud formation model. CARMA calculates the equilibrium cloud particle-size distribution by solving the 1D discretized continuity equation for aerosol particles that experience vertical transport due to sedimentation and eddy diffusion and production and loss due to particle nucleation (homogeneous and heterogeneous), condensation, evaporation, and coagulation. CARMA has been previously used to investigate condensate cloud formation on Earth (e.g., Ackerman et al. 1993; Jensen & Toon 1994; Ackerman et al. 1995), Venus (e.g., James et al. 1997; McGouldrick & Toon 2007; Gao et al. 2014), Mars (e.g., Colaprete et al. 1999), and exoplanets (e.g., Gao et al. 2018; Powell et al. 2019; Gao et al. 2020). CARMA has also been used to model photochemical hazes on Titan (Toon et al. 1992), Pluto (Gao et al. 2017), ancient Earth (Wolf & Toon 2010), and warm Jupiters (Adams et al. 2019). In order to make our use of CARMA computationally tractable, we divide each planet into two zones and calculate averaged temperature and K_{zz} profiles for each zone as described in Section 3.2 (see also Figure 3). We do not consider photochemical hazes here, as the
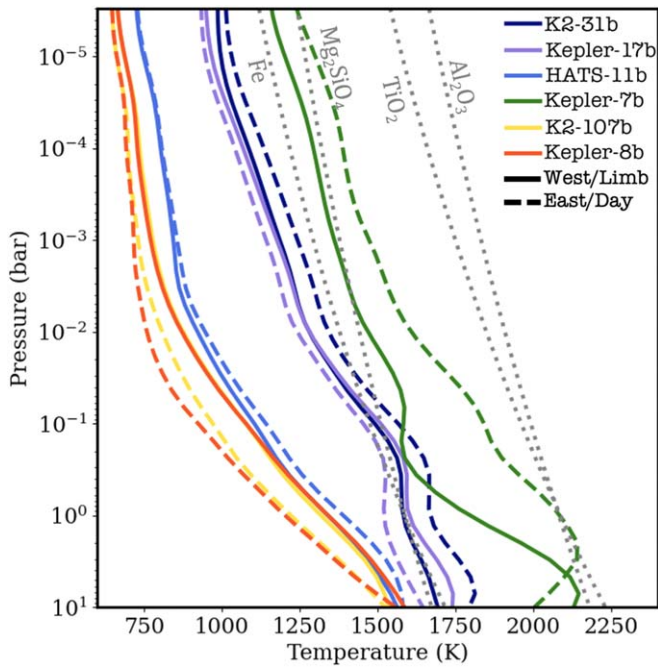
Figure 3. Condensation curves (dashed gray) of Fe, Al_2O_3, TiO_2, and Mg_2SiO_4 clouds compared with the two-zone model-averaged temperature profiles (see Section 3.2). Dayside (solid) and western limb (dashed) are shown for each planet: K2-107b (yellow), Kepler-8b (orange), HATS-11b (blue), K2-31b (navy), Kepler-17b (purple), and Kepler-7b (green).

planets in our sample lie above the temperature range where these hazes are expected to form (Lodders & Fegley 2002; Kawashima & Ikoma 2019; Gao et al. 2020).

In the CARMA model, the formation of condensate clouds begins with either homogeneous or heterogeneous nucleation. Cloud particles undergo homogeneous nucleation when stable clusters of condensate molecules form and grow directly from the vapor. The rate is controlled by the material properties of the condensate, such as its molecular weight and surface energy, and the flux of molecules to the cluster, which depends on the abundance of condensate vapor. Under the same supersaturation and local temperature, high-surface-energy and high-molecular-weight materials tend to nucleate more slowly than low-surface-energy and low-molecular-weight materials. Unlike homogeneous nucleation, heterogeneous nucleation involves the formation of stable clusters on condensation nuclei, or foreign surfaces, which are provided by other aerosol particles in the atmosphere. The size and abundance of these particles strongly impact the rate of heterogeneous nucleation. The nucleation rate is also dependent on the interaction between the condensate and the surface, characterized by the contact angle between the surface and the condensate cluster, the energy needed by a condensate molecule to desorb from the surface, and the oscillation frequency of the condensate molecule on the surface, which is related to the desorption energy (Pruppacher & Klett 1978).

Unlike in Virga, which assumes a log-normal particle-size distribution, particle-size distributions in CARMA are resolved using mass bins and can change over time via condensation, evaporation, and coagulation. The former two rates are dependent on the flux of condensate molecules and the rate at which particles may conduct away the latent heat released upon condensation. Coagulation, or growth via physically sticking upon the collision of particles, is also considered. Each mass bin corresponds to

particle masses twice that of the previous bin. We use 65 bins in our model, with the mass in the first bin corresponding to particles with radii of 0.1 nm for all species.

2.5. Cloud Compositions

For the Virga cloud modeling in this study, we are only interested in cloud species that are expected to be abundant in these atmospheres and which condense at relatively low pressures (approximately 1 bar). We identify three cloud species that are likely to be important based on comparing the species' condensation curves to the planets' temperature-pressure profiles (Figure 3; also see Ackerman & Marley 2001; Morley et al. 2012): Mg_2SiO_4, Al_2O_3, and TiO_2. This assumes that all SiO goes into Mg_2SiO_4 rather than SiO_2 or $MgSiO_3$. The inclusion of SiO_2 would require a different modeling framework including kinetic condensation. We plot the optical depths in the Kepler bandpass (shown in Figure 6) for these species as a function of pressure as computed by Virga at a representative location on the planet K2-107b in Figure 4. Although some previous studies of spatially inhomogeneous cloud formation in hot Jupiters also included sulfide clouds (e.g., Parmentier et al. 2016), recent microphysical cloud models (Powell et al. 2019; Gao et al. 2020) indicate that the high surface energy of sulfide condensates makes homogeneous nucleation unlikely. This conclusion is in good agreement with observational data indicating that the observed cloud opacity for more moderately irradiated hot Jupiters is well matched by models without sulfide condensates (e.g., Chachan et al. 2019; Gao et al. 2020). We therefore exclude sulfide condensates from our Virga models. Fe is also a potentially important condensate but, like the sulfides, previous microphysical modeling suggested that Fe cloud formation proceeds slowly due to Fe's high surface energy (Gao et al. 2020). On the other hand, Fe has been considered a major cloud component in many previous works (Sudarsky et al. 2003; Fortney 2005; Helling et al. 2008; Marley et al. 2013; Marley & Robinson 2015). Therefore, while our nominal Virga models will not include Fe, we will consider another set of simulations where Fe is included to explore its impact on our predicted albedos.

For the CARMA simulations in this study, we use the same model setup as in Gao et al. (2020) where clouds of TiO_2, Al_2O_3, Fe, Mg_2SiO_4, Cr, MnS, Na_2S, ZnS, and KCl are allowed to form. However, as previously discussed, in practice only Mg_2SiO_4, Al_2O_3, and TiO_2 form in any significant abundance. Of these three species, Mg_2SiO_4 is particularly unlikely to undergo homogeneous nucleation, as it is not abundant in the vapor phase. Instead, it is the product of a thermochemical reaction between Mg, SiO, and H_2O (e.g., Visscher et al. 2010). Similarly, Al_2O_3 does not exist in the gaseous phase as other aluminum oxide species will be more stable (e.g., Patzer et al. 2005). As in Gao et al. (2020), we allow these two species to heterogeneously nucleate on homogeneously nucleated TiO_2 seeds. Though Fe is permitted to both homogeneously and heterogeneously nucleate (on TiO_2 seeds), the high surface tension of Fe prevents significant Fe cloud formation.

2.6. Computing Optical Albedos with PICASO

We use the outputs from the cloud codes Virga and CARMA to calculate the single-scattering albedos, asymmetry parameters,
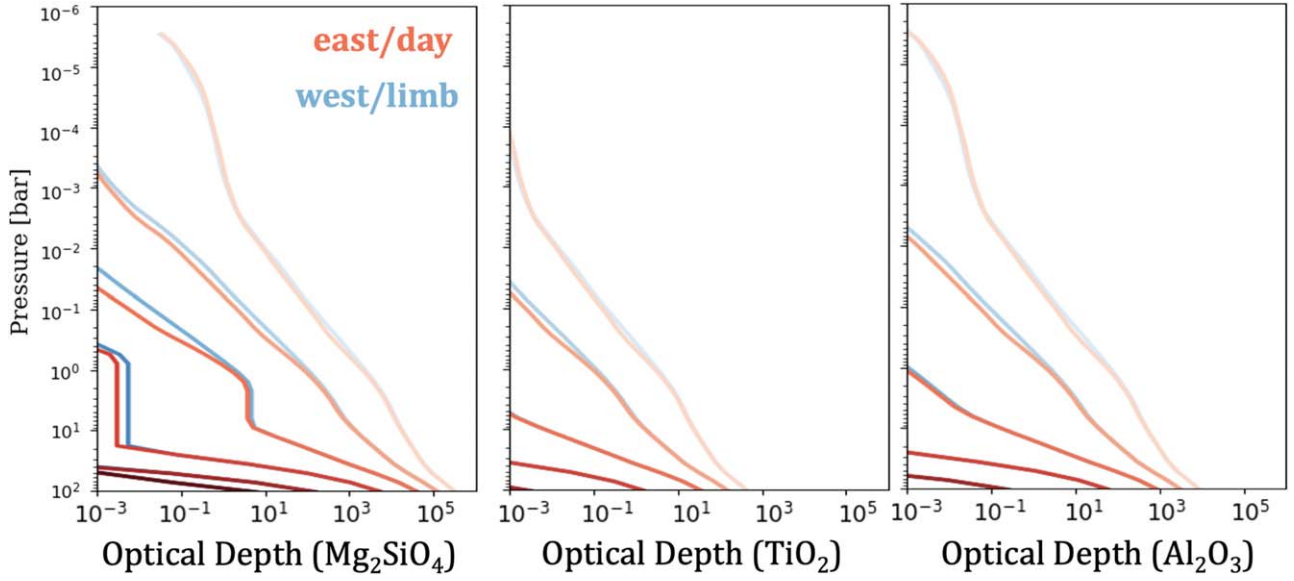
Figure 4. Nadir optical depths (integrated over the Kepler bandpass) for three condensate species in our `Virga` model of K2-107b. From left to right: Mg_2SiO_4, TiO_2, Al_2O_3. Each panel shows two representative grid points: blue corresponds to a western grid point centered at $-60°$ W, $8°$ N and red corresponds to a dayside grid point centered at $42°$ E, $8°$ N. The value of f_{sed}, which ranges from 0.03 to 6.0, is indicated by the shading of each line, where the lightest shades correspond to the smallest values and darkest shades represent the largest values of f_{sed}.

and optical depths for each pressure layer at each location in the atmosphere assuming Mie scattering. We then convert these quantities into wavelength-dependent albedos using The Planetary Intensity Code for Atmospheric Scattering Observations (`PICASO`; Batalha et al. 2019). This code is governed by the radiative transfer equation

$$I(\tau_i, \mu) = I(\tau_{i+1}, \mu)\exp\left(\frac{\delta\tau_i}{\mu}\right)$$
$$- \int_0^{\delta\tau_i} S(\tau'\mu)\exp(-\frac{\tau}{\mu})d\tau'/\mu, \qquad (2)$$

where $I(\tau_i, \mu)$ is the azimuthally averaged intensity emerging from the top of a layer, i, with opacity, τ_i, and outgoing angle, μ. $I(\tau_{i+1})\exp(\frac{\delta\tau_i}{\mu})$ is the incident intensity at the lower boundary of the layer attenuated by the optical depth within the layer, $\delta\tau$, and $S(\tau', \mu)$ is the source function integrated over all layers. The source function has two components: single-scattered and multiple-scattered radiation integrated over all diffuse angles:

$$S(\tau', \mu) = \frac{\omega}{4\pi}F_o P_{single}(\mu, -\mu_o)\exp(-\frac{\tau'}{\mu_s})$$
$$+ \frac{\omega}{2}\int_{-1}^{1} I(\tau', \mu')P_{multi}(\mu, \mu')d\mu', \qquad (3)$$

where ω is the single-scattering albedo and F_o is the incident flux. P_{multi} and P_{single} describe the phase function of the multiple and single scattering, respectively. P_{single} is an opacity-weighted combination of the Rayleigh phase function and a two-term Henyey–Greenstein phase function. P_{multi} requires integration over all diffuse angles, for which `PICASO` uses a $N = 2$ Legendre expansion. This approximation alone is inadequate to represent cases with high rates of forward scattering, so `PICASO` implements the delta-Eddington approximation to scale g, ω, and τ to more accurately capture the forward scattering peak.

`PICASO` considers the extinction from three opacity sources in order to calculate the geometric albedo as a function of wavelength: molecular absorption, Rayleigh scattering, and scattering by clouds. We show a representative calculation of these three opacity sources as a function of wavelength in Figure 5. To describe the phase-dependence, `PICASO` computes the emergent intensity from the disk at multiple plane-parallel facets, where each has its own incident and outgoing angles. `PICASO` uses the Chebyshev–Gauss integration method to integrate over all emergent intensities. We integrate the wavelength-dependent geometric albedo over the Kepler response function for each point in our 10×10 grid and then integrate again over the dayside hemisphere in order to obtain a geometric albedo that we can compare with the Kepler measurements. We have run sensitivity tests that demonstrate that a higher resolution grid (20×20 grid) yields comparable results.

2.7. Effect of Simplifying Model Assumptions

In this study we do not consider radiative feedback from clouds, which might affect our albedo predictions. Clouds can alter the planet's global thermal structure in several ways. First, they can reduce the amount of heating on the dayside by increasing the planet's Bond albedo. Second, they can suppress cooling on the nightside by preventing the reradiation of infrared light to space. Parmentier et al. (2021) and Roman et al. (2021) ran grids of 3D GCM models incorporating radiative feedback from clouds spanning a range of incident fluxes. They found that the presence of reflective clouds on the dayside resulted in lower global temperatures, while the presence of nightside clouds inhibited cooling, causing a 100–200 K global increase in temperature. With the possible exception of Kepler-7b (see Section 4.2.1), we expect that such shifts in temperature would not substantially alter the pressures of the cloud decks or reduce their horizontal extent for the planets examined here.
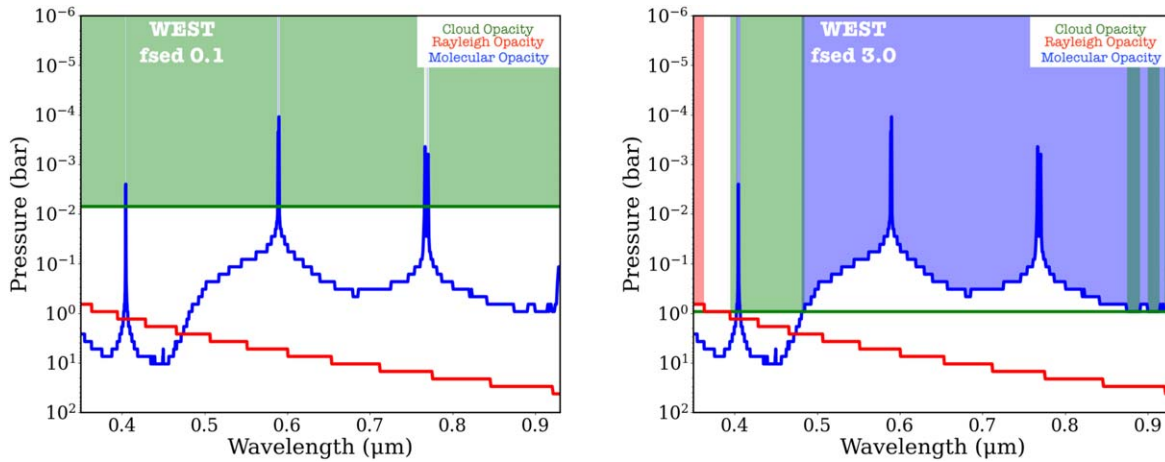
Figure 5. Pressure level (bar) of unit optical depth for Rayleigh scattering (pink), cloud opacity (green), and molecular opacity (blue) as a function of wavelength for a single grid point ($-60°$W, $8°$ N) in the `Virga` model of hot Jupiter K2-107b. f_{sed} of 0.1 is shown on the left and 3.0 on the right. The shaded regions indicate the dominant opacity source as a function of wavelength. This is the same grid point shown in Figure 4.

We also note that, in this study, our 3D atmospheric circulation models are decoupled from our cloud models. While this does enable more flexibility in exploring different cloud species and sedimentation parameters in both `Virga` and `CARMA`, cloud formation and transport is ultimately a coupled process between advection, radiation, and chemistry. Previous studies that couple cloud microphysical models and atmospheric circulation models (e.g., Lee et al. 2015; Lines et al. 2018) suggest that zonal (east/west) and/or meridional (north–south) transport of cloud particles from colder regions of the atmosphere could lead to high cloud-particle number densities, even on the hotter dayside, which could in turn enable more cloud nucleation and growth. These processes will only affect our dayside albedo predictions if the planet in question has large dayside temperature (and hence albedo) gradients with longitude or latitude. We revisit both of these assumptions (radiative feedback and cloud microphysics coupled to circulation) in Section 4.2, where we discuss their implications for individual planets in light of our model results.

3. Results

The SPARC/MITgcm models indicate that the day–night temperature contrasts for the six planets in our sample vary in magnitude (Figure 2). As expected, the hottest region on the dayside in all six models is located to the east of the substellar point. This shift is caused by eastward equatorial winds, which transport heat to the planet's nightside (e.g., Showman et al. 2020, and references therein).

Kepler-7b has the largest thermal gradient of all the planets in our sample, followed by K2-31b and Kepler-17b; this is because the former has a relatively low surface gravity (approximately $4\,\mathrm{m\,s^{-2}}$) and the latter two have the shortest orbital periods in the sample.

Kepler-7b has the largest thermal gradient of all the planets in our sample, followed by K2-31b and Kepler-17b; this is because the former has a relatively low surface gravity (approximately $4\,\mathrm{m\,s^{-2}}$) and the latter two have the shortest orbital periods in the sample. Our models indicate that Kepler-7b is also warmer at depth than the other planets in this sample. This is expected, as Kepler-7b has the lowest surface gravity of the six planets and under hydrostatic equilibrium the gradient

of temperature with respect to pressure is related to the inverse of the surface gravity (e.g., Gao et al. 2018).

3.1. Virga Model Results

In order to determine the effect of the clouds on the albedo, we must first calculate their vertical extent at each location in our model grid. In our `Virga` equilibrium cloud models, the vertical extent of the clouds is controlled by our choice of f_{sed}. Taking K2-107b as a representative example, Figure 4 indicates that Mg_2SiO_4 clouds reach a unit optical depth near 1 mbar for the lowest f_{sed} value, 0.03, and near 50 mbar for $f_{sed} = 0.1$. These clouds will only contribute to the albedo at wavelengths where they reach optical depth unity at lower pressures than Rayleigh scattering or molecular opacity (Figure 5). This means that clouds will have a greater effect at wavelengths where the combined molecular and Rayleigh scattering opacity is lower. We show the effect of varying f_{sed} on the wavelength-dependent albedo of K2-107b in Figure 6. As f_{sed} decreases and the clouds extend to lower pressures, the cloud opacity contributes most to the overall albedo for an increasingly large fraction of the Kepler bandpass.

We next examine how the contribution of clouds to the band-integrated albedo varies across the dayside atmosphere. In Figure 7, we show the 10×10 grid of albedos in the Kepler bandpass for each planet as a function of f_{sed}. We find that the three planets with the greatest temperature variation as a function of longitude (Kepler-7b, K2-31b, and Kepler-17b) also have relatively large albedo variations across their dayside atmospheres for low-to-intermediate f_{sed} values. Once f_{sed} increases above 0.3, the clouds remain confined below the optical depth unity level of molecular absorbers, such that the presence or absence of clouds does not affect the observed albedo. These three planets appear brighter on their western limbs than in the east, in good agreement with the albedo maps derived from the Kepler phase curve for Kepler-7b (Demory et al. 2013) and other planets with comparable equilibrium temperatures (Shporer & Hu 2015). In contrast to these three planets, HATS-11b, K2-107b, and Kepler-8b all appear to have fairly homogeneous albedos, as expected based on their more homogeneous thermal structures.

Lastly, we compare the hemisphere-averaged dayside albedo in the Kepler bandpass as a function of f_{sed} to the measured
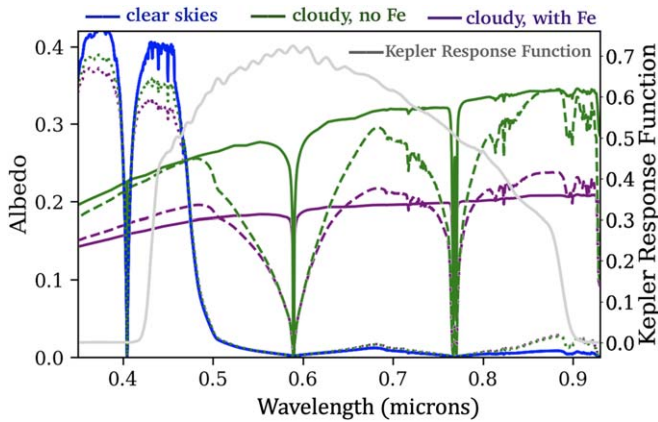
Figure 6. Hemisphere-averaged albedo of K2-107b as a function of wavelength for a clear atmosphere (blue) and cloudy atmospheres of varying f_{sed} values (green; 0.03 as a solid line, 0.1 as a dashed line, and 0.3 as a dotted line). Cloudy atmospheres including Fe condensates are shown in purple. All cloud distributions are computed using Virga. The Kepler response function is overplotted in gray.

dayside albedo for each planet (Figure 8). We find that K2-31b and K2-107b are best described by models with large values of f_{sed} or (equivalently) clear atmospheres, indicating that any reflective clouds present in these atmospheres do not extend above the level of unit molecular opacity. Kepler-17b and Kepler-8b are best matched by models with intermediate f_{sed} values, implying that their albedos are moderately enhanced by cloud opacity. HATS-11b is best matched by models with low f_{sed} values, corresponding to a high, vertically extended reflective cloud layer spanning a wide range of longitudes. No f_{sed} value is able to reproduce the high observed albedo for Kepler-7b, which our models indicate is too warm for bright Mg_2SiO_4 clouds to form over much of the dayside. Instead, our models indicate that the dayside of Kepler-7b is dominated by deep Al_2O_3 clouds at pressures of around a bar. The addition of iron clouds do not greatly change our results except for decreasing the albedos of low f_{sed} models, as iron clouds sink below the photosphere for higher f_{sed}'s. We list the observed albedos and the predicted albedos as a function of f_{sed} in Table 2. We find that the hemisphere-integrated albedo over the Kepler bandpass is very sensitive to the assumed value of f_{sed}.

3.2. Comparison to CARMA Microphysical Models

We find that dayside albedos can vary significantly depending on the assumed sedimentation efficiency (e.g., Figure 7). We therefore use these maps to divide each planet into two zones, and then utilize the more computationally demanding CARMA microphysical cloud model to solve for the vertical extent of the clouds and corresponding albedo in each zone.

Our Virga albedo maps indicate that a subset of the planets in our sample are likely to have spatially inhomogeneous Mg_2SiO_4 clouds located near their western limbs. Although it would be computationally prohibitive to run a separate CARMA model for each point in the 10×10 grid, we can nonetheless capture this cloud structure using a more computationally tractable two-zone model. We define a threshold value in longitude for each planet based on the albedo distributions found by Virga as shown in Figure 7 and in Table 3. We determine the longitude range defining the two zones (a western zone and a dayside zone) as the division that yields the

greatest difference in albedo at mid-latitudes as determined from the Virga albedo maps. Occasionally the western zone includes a limb region in the east; see Table 3 for a list of the zone definitions for each planet. The resulting zonally averaged pressure-temperature profiles are plotted in Figure 3. We run a separate CARMA model for each zone, and also run Virga models for the same zones in order to facilitate comparisons between the two models. In the discussion below, we limit our comparisons to these two-zone Virga models unless otherwise noted.

When comparing the two models, it is important to note that they predict distinct particle compositions. While Virga assumes that particles nucleate homogeneously, CARMA predicts that the Mg_2SiO_4 condensates will nucleate heterogeneously onto TiO_2 cores (see Section 2.5). We find that accounting for this TiO_2 core when we calculate the single-scattering albedos for the Mg_2SiO_4 particles in our CARMA models results in a lower single-scattering albedo than when we repeat the calculation for pure Mg_2SiO_4 particles, which return single-scattering albedo profiles of greater than 0.96. For comparison, we refer the reader to Figure 9; a single value for single-scattering albedo is not representative of heterogeneous particles, which are sensitive to the core mass fraction of TiO_2. However, even after accounting for this effect we find that the species-averaged single-scattering albedo shown in Figure 9 for our CARMA models with heterogeneous particles is still comparable to the Virga models with f_{sed} equal to 0.1 (Figure 10).

When we calculate the hemisphere-integrated albedos for these planets from the CARMA models we find that they generally lie within the range of Virga predictions for varying f_{sed} (see Figure 8 and Table 3). In Figure 8, we show the hemisphere-integrated albedos from the full-resolution Virga model from Section 2.3 rather than the two-zone model discussed in this section.

We find that K2-107b and HATS-11b appear to have the brightest hemisphere-integrated CARMA albedos, with values consistent with those of the lowest f_{sed} ($0.03 - 0.1$) Virga models. Kepler-8b, Kepler-17b, and K2-31b have somewhat lower predicted CARMA albedos, more comparable to the f_{sed} of 0.3 Virga models. Kepler-7b is a notable exception, as our CARMA model predicts an albedo that is higher than that of the smallest f_{sed} Virga model.

4. Discussion

4.1. Comparison to Previous Modeling Efforts

We can compare our results to generic grids of cloudy GCM models in the published literature. First, we note that our GCM outputs for Kepler-7b roughly agree with those shown in Oreshenko et al. (2016), and the general distribution of our silicate and corundum clouds agrees with the modeling results of Roman & Rauscher (2019).

Roman et al. (2021) investigated planetary albedos using a grid of GCMs with varying irradiation temperature and surface gravity. The closest equivalent models in their grid are for a planet with an irradiation temperature of either 2500 K (equilibrium temperature of 1500 K) or 2750 K (equilibrium temperature of 1700 K) and a surface gravity of $10 \, m \, s^{-2}$. We compare to their nucleation-limited models, which also exclude iron and sulfide condensates.
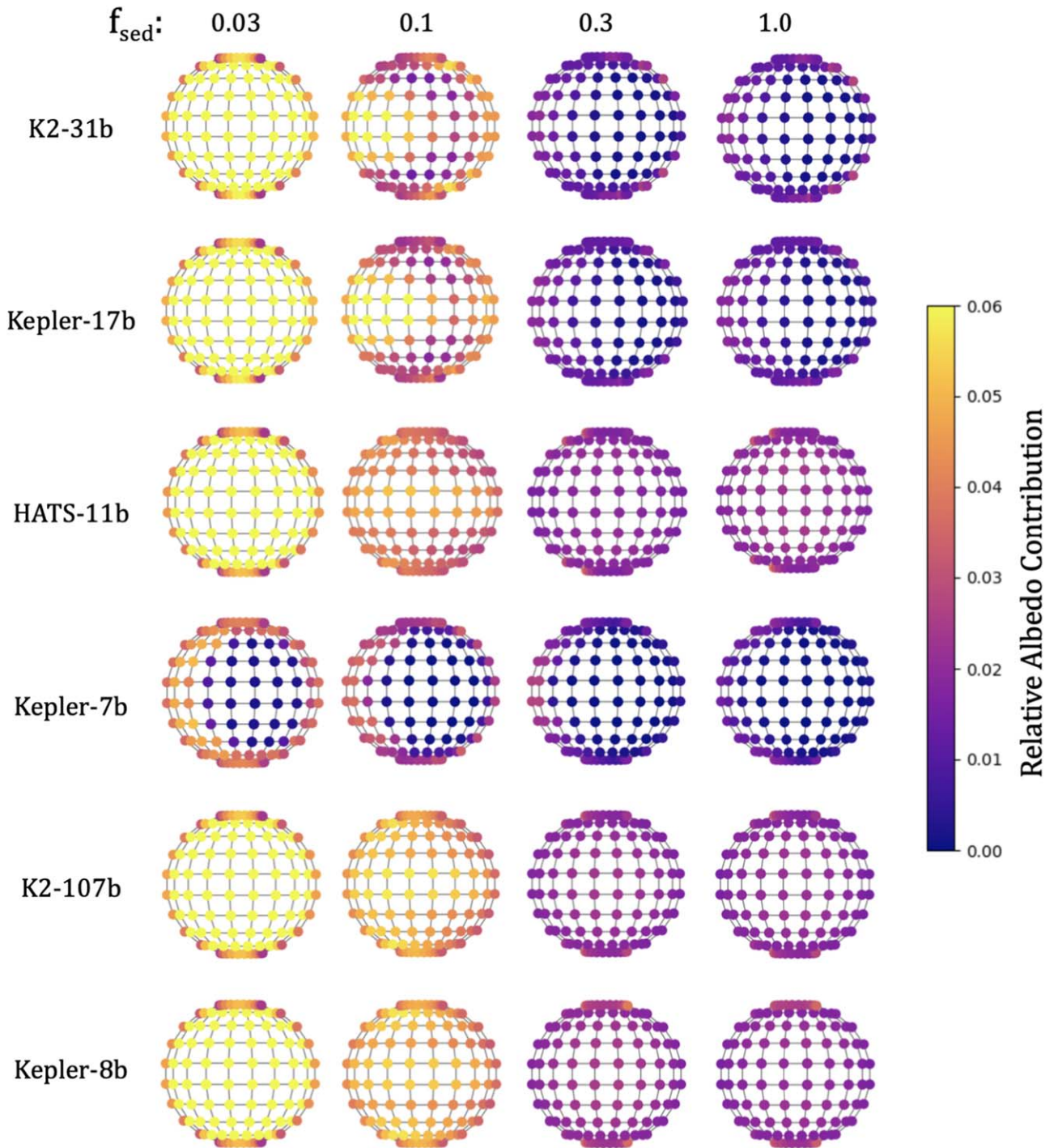
Figure 7. Relative dayside albedo contribution at each grid point including appropriate geometric weights. Planets are sorted by increasing equilibrium temperature from top to bottom, and sorted by increasing f_{sed} (0.03, 0.1, 0.3, and 1.0) from left to right. We omit f_{sed} values of 3.0 and 6.0 from the figure, as the clouds in these models reside below the level of unit molecular albedo, and thus the albedo remains roughly unchanged compared to the $f_{sed} = 1.0$ case. The relative albedo contributions are all smaller than the face-integrated albedo by roughly a factor of π; summing over the points yields the integrated albedo. The models include three cloud species: Mg_2SiO_4, Al_2O_3, and TiO_2.

The models presented in Roman et al. (2021) assume a fixed pressure-dependent particle size for the clouds, with a size of 0.1 μm at the top of the atmosphere that increases exponentially with increasing pressure for pressures greater than 10 mbar. Since their equilibrium cloud models do not solve for the vertical extent of the cloud layers, they present two cases corresponding to compact (cloud tops limited to 1.4 scale heights above the cloud base) and vertically extended (cloud-top pressure of 0.1 mbar) cloud layers. Unlike our models, they account for radiative

feedback from these clouds when solving for the temperature structure of the atmosphere. These models indicate that compact cloud layers will result in relatively low and uniform dayside albedos, in good agreement with our results (Figure 7). Their vertically extended cloud models exhibit a range of optical spherical albedos between 0.2 and 0.3, with lower values for the higher temperature model as the reflective silicate clouds become increasingly confined to the cooler western region of the atmosphere. This also agrees with the qualitative picture from
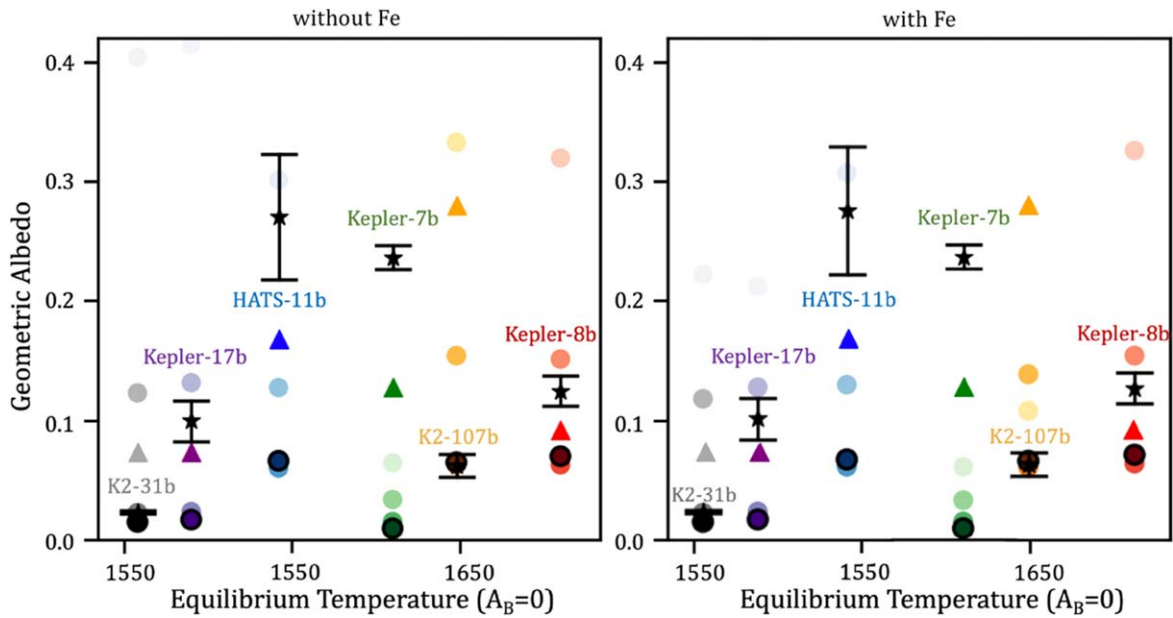
Figure 8. Geometric albedo predictions in the Kepler optical bandpass compared with published albedo measurements as a function of equilibrium temperature. Albedo predictions from the full-resolution `Virga` models are shown as circles, where the shading indicates the f_{sed} value, going from 0.03 (light) to 6.0 (dark). Kepler albedo measurements are shown as stars while the predicted albedos from the two-zone `CARMA` models are shown as triangles. The left panel excludes Fe in `Virga` calculations, while the right panel includes Fe condensates.

Table 2
Hemisphere-averaged Albedos from `Virga` Models as a Function of f_{sed}[a]

Planet	Measured	Clear	0.03	0.1	0.3	1.0	3.0	6.0	0.1, with Fe
K2-31b	0.023 ± 0.002	0.015	0.404	0.123	**0.023**	0.015	0.015	0.015	0.115
Kepler-17b	0.099 ± 0.017	0.017	0.416	**0.131**	0.023	0.017	0.017	0.017	0.125
HATS-11b	0.270 ± 0.052	0.066	**0.301**	0.127	0.060	0.066	0.066	0.066	0.127
Kepler-7b	0.194 ± 0.013	0.009	**0.064**	0.034	0.015	0.010	0.009	0.009	0.030
K2-107b	0.062 ± 0.010	0.065	0.333	0.154	**0.063**	0.065	0.065	0.065	0.134
Kepler-8b	0.124 ± 0.013	0.069	0.319	**0.151**	0.063	0.070	0.070	0.070	0.151

Note.
[a] Bolded values indicate the simulated `Virga` albedo that best matches the Kepler eclipse observations.

Table 3
Hemisphere-averaged Dayside Albedos from `CARMA` Models

Planet	Measured	Clear	West	Day	Day Zone[a]	Integrated
K2-31b	0.023 ± 0.002	0.015	0.085	0.054	$[-17°W, 51°E]$	0.073
Kepler-17b	0.099 ± 0.017	0.017	0.074	0.069	$[0°E, 90°E]$	0.073
HATS-11B	0.270 ± 0.052	0.066	0.169	0.165	$[51°E, 90°E]$	0.168
Kepler-7b	0.194 ± 0.013	0.009	0.199	0.034	$[-38°W, 51°E]$	0.128
K2-107b	0.062 ± 0.010	0.065	0.233	0.229	$[51°E, 90°E]$	0.280
Kepler-8b	0.124 ± 0.013	0.069	0.082	0.109	$[51°E, 90°E]$	0.092

Note.
[a] Eastern/day zone boundaries are listed in the table. The western/limb zone is defined as the region excluded by the dayside definition.

our models, which span an equivalent range of albedos. They conclude that their optical albedos for the nucleation-limited case are dominated by silicate cloud particles, consistent with our conclusions here.

Parmentier et al. (2016) and Parmentier et al. (2021) considered GCMs spanning a wide range of equilibrium temperatures. In Parmentier et al. (2016), the clouds are post-processed (i.e., they do not include cloud radiative feedback in the GCM models), and they model the condensation of a wide range of cloud species. These models predict that $MgSiO_3$ and $CaTiO_3$ clouds should

dominate the dayside optical albedo for planets with equilibrium temperatures between 1500 and 1700 K. In Parmentier et al. (2021) they incorporate cloud radiative feedback for the condensation of a single cloud species, MnS, but the treatment of silicate clouds is similar to Parmentier et al. (2016). For that reason, we focus on Parmentier et al. (2016) for our comparison. In this study they assume a small fixed-particle-size distribution centered at 0.1 μm and a cloud-top pressure of 1 microbar, which yields geometric albedos greater than 0.5 in the Kepler bandpass for planets of approximately 1500 K equilibrium temperature.
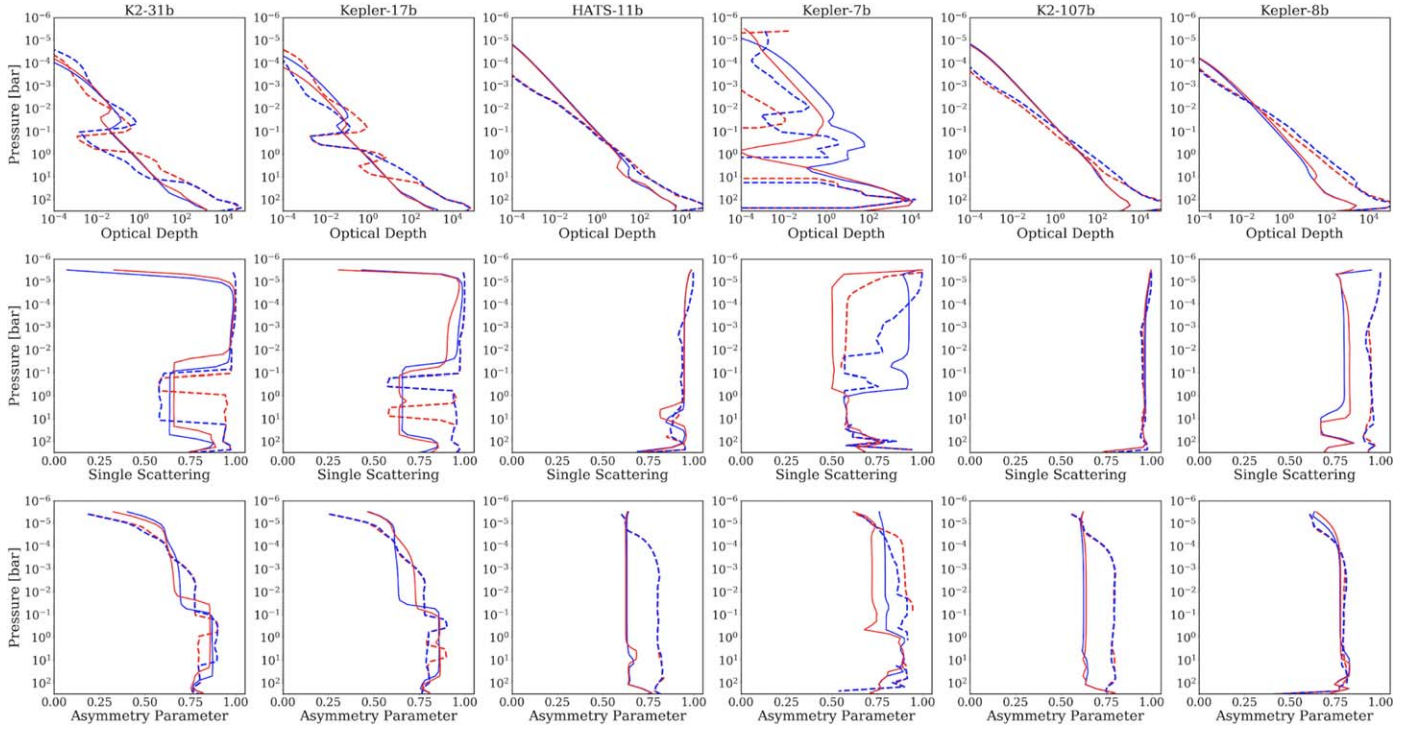
Figure 9. Optical depth (left), single-scattering albedo (center), and asymmetry parameter (right) as a function of pressure for the two-zone `Virga` (dashed; f_{sed} fixed to 0.1) and `CARMA` (solid) models, calculated by dividing the dayside hemisphere into a dayside (red) and western (blue) zone (see Section 3.2). Each row corresponds to a different planet, sorted left to right by increasing equilibrium temperature.
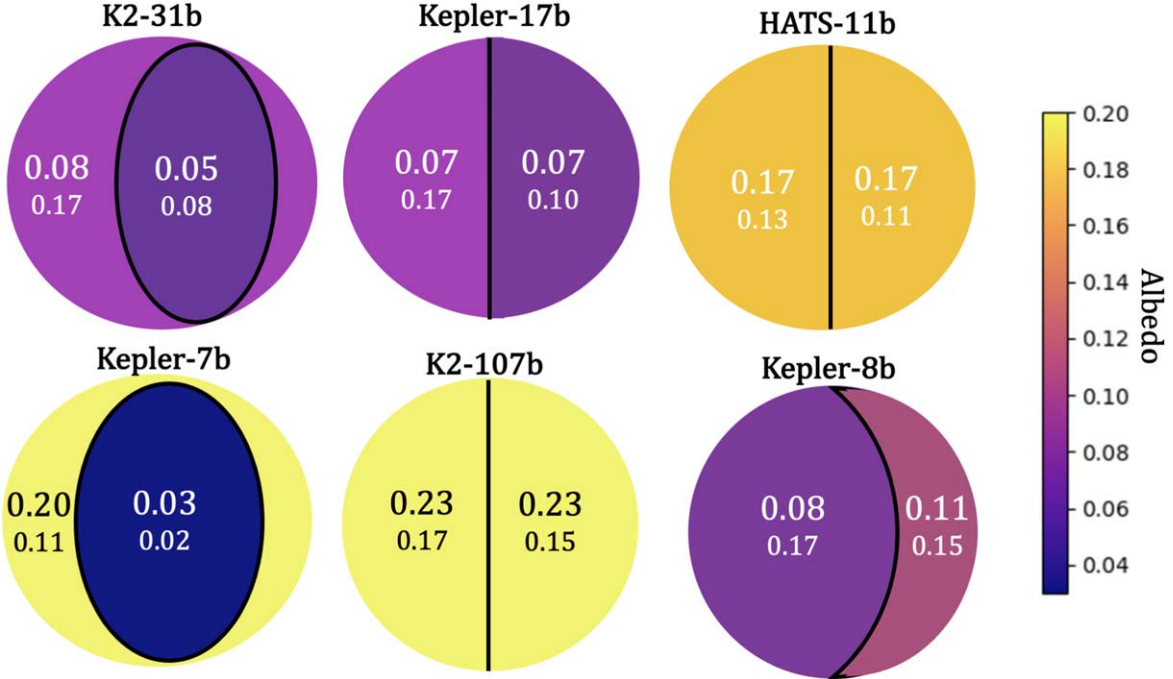

Figure 10. Dayside and western zone albedos from the `CARMA` models integrated over the Kepler bandpass. `Virga` model albedos with f_{sed} equal to 0.1 are listed below for comparison. Both sets of models are calculated in two zonally averaged regions, defined in Table 3. Planets are sorted from left to right and top to bottom by increasing equilibrium temperature.

This value is much higher than both our albedos and those reported by Roman et al. (2021), and is most likely due to the very low cloud-top pressure assumed in these models. They invoke a cold trap for silicates to reduce the albedo, while we predict that changing the cloud vertical extent can achieve a similar difference in observable albedo.

4.2. Comparison to Published Kepler Albedos

Our results show that, with the exception of Kepler-7b, it is possible to match the observed optical geometric albedos for all of the planets in our sample using either `Virga` or `CARMA` models. However, no single model (`Virga` at a fixed f_{sed} or

CARMA) can explain the observed albedos of all six planets. Although the albedo predictions from the CARMA models are broadly consistent with those of the Virga models, neither model is able to reproduce or explain the observed planet-to-planet variations in dayside albedo. This suggests that accounting for differences in equilibrium temperature, host-star spectral type, surface gravity, and rotation rate alone are not sufficient to capture the observed diversity of hot Jupiter albedos in this temperature range. We discuss our results in more detail on a planet-by-planet basis below.

4.2.1. Kepler-7b: Spatially Resolved Clouds

Our CARMA and Virga models both indicate that Kepler-7b's relatively bright dayside albedo is dominated by reflection from the region near the western limb, in good agreement with spatially resolved albedo constraints from phase-curve observations (Demory et al. 2013; Heng et al. 2021). This underscores the importance of using spatially resolved cloud models for tidally locked hot Jupiters. We note that there is some tension between our model predictions and the observational data, as fits to Kepler-7b's optical phase curve indicate that the bright reflective western zone extends as far as $10° ± 6°$ west of the substellar point (Muñoz & Isaak 2015; Heng et al. 2021). Our Virga models predict that the atmosphere will only be cool enough for Mg_2SiO_4 clouds to condense in the two westernmost longitude bins (extending from the terminator to approximately $38°$ west of the substellar point; see Figure 7 and Table 3). This is likely why our models underpredict Kepler-7b's optical geometric albedo.

We consider two possible explanations for this discrepancy. Zonal transport of cloud particles from the western-limb region could increase the albedo in adjacent longitudes where the atmosphere is otherwise too warm for them to condense (see Section 2.7). However, our models for Kepler-7b prefer small cloud particles with a large vertical extent; these small particles might have a relatively short lifetime in the hotter substellar region of the dayside atmosphere. Instead, perhaps small particles transported meridionally could nucleate and grow in bands at high latitudes (Lines et al. 2018). Ultimately, this planet would be an interesting test case for microphysical transport models (e.g., Lee et al. 2015; Lines et al. 2018), which can explicitly quantify the timescales of these processes and predict the resulting horizontal distribution of cloud particles.

Alternatively, if Kepler-7b's dayside is cooler than predicted by our GCM, Mg_2SiO_4 would be able to condense over a wider range of longitudes. Our GCMs do not account for reflectivity from clouds when calculating the effect of incident starlight on the dayside atmosphere; this effect might reduce the magnitude of dayside heating and result in globally lower temperatures (Lines et al. 2018; Roman & Rauscher 2019; Roman et al. 2021). However, if the clouds extend over a significant fraction of the planet's nightside it could result in net global warming, as they would act to reduce the amount of energy that can be radiated to space in this region (Roman & Rauscher 2019; Parmentier et al. 2021; Roman et al. 2021). For Kepler-7b, whose clouds extend over much of the western hemisphere, it is unclear which of these two competing effects would dominate. These explanations assume that the dayside-coverage area is the most significant limiting factor on the brightness of the dayside-integrated albedo. However, it is also important to consider factors that might increase the brightness of the cloudy region, including a larger vertical extent for the clouds or brighter cloud particles. We discuss how porous particles may increase HATS-11bs dayside albedo in Section 4.2.3; this same explanation might also apply to Kepler-7b.

4.2.2. K2-31b and K2-107b Do Not Host High-altitude Reflective Cloud Layers

The observed albedos of K2-31b and K2-107b are relatively low, and are well matched by Virga models with clear skies and/or deep clouds (i.e., those with opacities dominated by molecular absorption). For K2-31b, the contribution of clouds to the albedo is negligible for f_{sed} of 0.3 and larger. For K2-107b, we obtain a comparable result for f_{sed} of 1.0 and larger. This suggests that both of these planets may have relatively efficient sedimentation (deep clouds), or alternatively that they have relatively little condensable material in their atmospheres (perhaps corresponding to a relatively low atmospheric metallicity). If the lack of clouds is due to efficient sedimentation, this would appear to contradict predictions from our microphysical CARMA models, which track the sedimentation of cloud particles explicitly and predict albedos that are a factor of two or more higher than the observed values for these two planets.

Our CARMA models utilize vertical mixing rates calculated from our GCMs. If these mixing rates are overestimates of the true values, we might expect any clouds near the day–night terminator on these planets to also be relatively compact. If this is the case, the transmission spectra of these two planets should show relatively strong absorption features. Although K2-31b has a high surface gravity and is therefore a more challenging target for transmission spectroscopy, K2-107b might be accessible to future space telescopes like the James Webb Space Telescope. More broadly, the sedimentation rates calculated from GCMs and CARMA could be tested with comparisons to transmission spectra from ongoing surveys (Sing et al. 2016; Crossfield & Kreidberg 2017; Fu et al. 2017). If CARMA models underestimate the sedimentation efficiency for other planets, the disagreement should be detectable in these data, which are very sensitive to the vertical distribution of cloud particles near the limb. To date, most planets appear to be well matched by CARMA-model predictions (e.g., Chachan et al. 2020; Gao et al. 2020), indicating that such model–data disagreements may be relatively rare.

4.2.3. HATS-11b, K2-31b, and K2-107b Have Reflective Dayside Clouds

The measured Kepler albedo for HATS-11b ($0.27 ± 0.05$) is brighter than that of Kepler-7b, in good agreement with our model predictions. This planet is cooler than Kepler-7b, with a smaller day–night temperature gradient. As a result, our models predict a global reflective dayside cloud layer for small f_{sed} values, and our hemisphere-integrated Virga albedo for the f_{sed} of 0.03 model is within 1σ of the measured value. This is an unusually small value of f_{sed}, compared to the other planets' best-fit value, while more typical values of 0.1 and larger underestimate the observation. The CARMA-model albedo is somewhat lower, but is still within 2σ of the observed value. If we wish to adapt our models to better match this planet's high dayside albedo, it likely would require increasing the predicted cloud opacity, such as by increasing the porosity of the cloud particles (Samra et al. 2020). Although increasing the atmospheric metallicity might also increase the cloud opacity, published models for other planets indicate that there is not a simple scaling between these two quantities (e.g., Morley et al. 2013;

Gao et al. 2018), and increasing the metallicity will also affect the global thermal structure (e.g., Kataria et al. 2015).

Our model predictions for Kepler-17b and Kepler-8b are also in reasonable agreement with the observed albedos. In both cases, an $f_{sed} = 0.1$ `Virga` model slightly overestimates the albedo while our `CARMA` model slightly underestimates the albedo. This may indicate that moderately bright/cloudy worlds have moderate sedimentation efficiencies. For Kepler-8b, both `CARMA` and `Virga` models predict that the planet will have relatively uniform cloud coverage in both latitude and longitude; we therefore do not need to consider further spatial variations in cloud number density and particle size. For Kepler-17b, the $f_{sed} = 0.1$ `Virga` model predicts an albedo gradient across the dayside atmosphere, but this gradient appears to be localized near the equatorial (low-latitude) region of the atmosphere. Our `CARMA` model predicts a relatively uniform albedo across the two zones, but this may be biased by our inability to resolve latitudinal gradients in the simplified two-zone model.

5. Conclusions

Optical secondary eclipse measurements made by Kepler reveal a wide range of geometric albedos for hot Jupiters with equilibrium temperatures between 1550 and 1700 K. We combine 3D GCMs with both equilibrium (`Virga`) and microphysical (`CARMA`) cloud models to explore whether 3D effects can explain these observations. We find that the predicted albedos from our `Virga` models are very sensitive to the assumed sedimentation efficiency (f_{sed}). We can compare these albedo predictions to results from our `CARMA` model, which use mixing rates calculated from the GCM models to predict the vertical extent and particle-size distributions of the clouds. We find that while the hemisphere-integrated `CARMA` albedos generally agree with the range of albedos predicted by `Virga`, there is no single f_{sed} value that consistently matches the `CARMA` predictions.

When we compare these model predictions to the measured Kepler albedos for each of the six planets in our sample, we find that the albedos of K2-31b and K2-107b are best matched by models that are either cloud-free or have very deep compact cloud layers (large f_{sed} values). Kepler-8b and Kepler-17b's optical albedos can be matched by moderately cloudy models (f_{sed} greater than 0.3). Both `Virga` and `CARMA` tend to underpredict the dayside albedos of the two most reflective planets in our sample, HATS-11b and Kepler-7b, which are best matched by `Virga` models with reflective Mg_2SiO_4 clouds extending to very low pressures ($f_{sed} = 0.03$); our `CARMA` model for HATS-11b predicts a slightly lower albedo value than the brightest `Virga` model, while our `CARMA` model for Kepler-7b predicts a slightly higher albedo value than `Virga`. Although HATS-11b has relatively uniform cloud coverage across the dayside, it is possible that other factors (such as a low particle porosity) might increase the dayside cloud opacity beyond the values predicted by our models.

Our models predict that the observed albedo of Kepler-7b should be lower than that of HATS-11b, in good agreement with the observations. Although a bright reflective cloud layer forms in the westernmost region of the dayside atmosphere, most dayside longitudes in Kepler-7b's atmosphere are too warm for Mg_2SiO_4 to condense, resulting in a lower hemisphere-averaged dayside albedo. Empirical constraints on the horizontal extent of the western cloudy region from phase-curve observations

indicate that it extends farther east than predicted by our models, hinting that a more detailed study of the planet that couples cloud microphysics and dynamics is required.

We conclude that the sample of optical albedos measured by Kepler represents a rich source of information for 3D cloud models, and that there is no single explanation for the observed diversity of albedos for the planets considered in this study. Future studies leveraging the large sample of transmission spectra of hot Jupiters could provide complementary constraints on the typical sedimentation efficiencies of their atmospheres, while additional complementary modeling studies exploring the coupled effects of atmospheric dynamics and cloud microphysics, as well as an exploration of the microporosity of cloud particles, would help to further illuminate the relative importance of these processes in explaining the high albedos of the brightest planets in our sample.

ORCID iDs

Danica J. Adams ⓘ https://orcid.org/0000-0001-9897-9680
Tiffany Kataria ⓘ https://orcid.org/0000-0003-3759-9080
Natasha E. Batalha ⓘ https://orcid.org/0000-0003-1240-6844
Peter Gao ⓘ https://orcid.org/0000-0002-8518-9601
Heather A. Knutson ⓘ https://orcid.org/0000-0002-5375-4725

References

Ackerman, A. S., Hobbs, P. V., & Toon, O. B. 1995, JAtS, 52, 1204
Ackerman, A. S., & Marley, M. S. 2001, ApJ, 556, 872
Ackerman, A. S., Toon, O. B., & Hobbs, P. V. 1993, Sci, 262, 226
Adams, D., Gao, P., de Pater, I., & Morley, C. V. 2019, ApJ, 874, 61
Adcrot, A., Campin, J.-M., Hill, C., & Marshall, J. 2004, MWRv, 132, 2845
Angerhausen, D., Huber, K., Mandell, A., et al. 2014, in Proc. IAU, Formation, Detection, and Characterization of Extrasolar Habitable Planets (Cambridge: Cambridge Univ. Press), 293
Arakawa, E. T., Williams, M. W., & Inagaki, T. 1977, JAP, 48, 3176
Barclay, T., Huber, D., Rowe, J. F., et al. 2012, ApJ, 761, 53
Barstow, J. K., Aigrain, S., Irwin, P. G. J., et al. 2014, ApJ, 786, 154
Batalha, N. 2020, natashabatalha/virga: Initial Release, v0.0, Zenodo, doi:10.5281/zenodo.3759888
Batalha, N. E., Marley, M. S., Lewis, N. K., & Fortney, J. J. 2019, ApJ, 878, 70
Bayliss, D., Hartman, J. D., Zhou, G., et al. 2018, AJ, 155, 119
Bell, T. J., Nikolov, N., Cowan, N. B., et al. 2017, ApJL, 847, L2
Bokeh Development Team 2014, Bokeh: Python library for interactive visualization, http://www.bokeh.pydata.org
Bonomo, A. S., Desidera, S., Benatti, S., et al. 2017, A&A, 602, A107
Burrows, A., Ibgui, L., & Hubeny, I. 2008, ApJ, 682, 1277
Chachan, Y., Jontof-Hutter, D., Knutson, H. A., et al. 2020, AJ, 160, 201
Chachan, Y., Knutson, H. A., Gao, P., et al. 2019, AJ, 158, 244
Colaprete, A., Toon, O. B., & Magalhães, J. A. 1999, JGRE, 104, 9043
Coughlin, J., & Lopez-Morales, M. 2012, ApJ, 143, 39
Crossfield, I. J. M., & Kreidberg, L. 2017, AJ, 154, 261
Demory, B.-O., de Wit, J., Lewis, N., et al. 2013, ApJL, 776, L25
Demory, B.-O., Seager, S., Madhusudhan, N., et al. 2011, ApJ, 735, L12
Desert, J.-M., Charbonneau, D., Fortney, J. J., et al. 2011, ApJS, 197, 11
Eigmuller, P., Gandolfi, D., Persson, C. M., et al. 2017, AJ, 153, 130

Esteves, L. J., De Mooij, E. J. W., & Jayawardhana, R. 2013, ApJ, 772, 51
Esteves, L. J., De Mooij, E. J. W., & Jayawardhana, R. 2015, ApJ, 804, 150
Evans, T. M., Pont, F., Sing, D. K., et al. 2013, ApJL, 772, L16
Fortney, J. J. 2005, MNRAS, 364, 649
Fortney, J. J., Cooper, C. S., Showman, A. P., Marley, M. S., & Freedman, R. S. 2006, ApJ, 652, 746
Fortney, J. J., Demory, B.-O., Désert, J.-M., et al. 2011, ApJS, 197, 9
Fraine, J., Mayorga, L. C., Stevenson, K. B., et al. 2021, AJ, 161, 269
Fu, G., Deming, D., Knutson, H., et al. 2017, ApJL, 847, L22
Gao, P., Fan, S., Wong, M. L., et al. 2017, Icar, 287, 116
Gao, P., Marley, M. S., & Ackerman, A. S. 2018, ApJ, 855, 86
Gao, P., Marley, M. S., Zahnle, K., Robinson, T. D., & Lewis, N. K. 2017, AJ, 153, 139
Gao, P., Thorngren, D. P., Lee, G. K. H., et al. 2020, NatAs, 4, 951
Gao, P., Zhang, X., Crisp, D., Bardeen, C. G., & Yung, Y. L. 2014, Icar, 231, 83
Goode, P. R., Qiu, J., Yurchyshyn, V., et al. 2001, GeoRL, 28, 1671
Goody, R., West, R., Chen, L., & Crisp, D. 1989, JQSRT, 42, 539
Grziwa, S., Gandolfi, D., Csizmadia, S., et al. 2016, AJ, 152, 132
Guillot, T., & Showman, A. P. 2002, A&A, 385, 156
Helling, C. 2019, AREPS, 47, 583
Helling, C., Dehn, M., Woitke, P., & Hauschildt, P. H. 2008, ApJL, 675, L105
Helling, C., Iro, N., Corrales, L., et al. 2019, A&A, 631, A79
Helling, C., Kawashima, Y., Graham, V., et al. 2020, A&A, 641, A178
Heng, K., & Demory, B.-O. 2013, ApJ, 777, 100
Heng, K., Morris, B., & Kitzmann, D. 2021, NatAs, 5, 1001
James, E., Toon, O., & Schubert, G. 1997, Icar, 129, 147
Jensen, E. J., & Toon, O. B. 1994, GeoRL, 21, 2019
Kataria, T., Showman, A. P., Fortney, J. J., et al. 2015, ApJ, 801, 86
Kataria, T., Showman, A. P., Lewis, N. K., et al. 2013, ApJ, 767, 76
Kataria, T., Sing, D. K., Lewis, N. K., et al. 2016, ApJ, 821, 9
Kawashima, Y., & Ikoma, M. 2019, ApJ, 877, 109
Kipping, D., & Bakos, G. 2011, ApJ, 733, 36
Kirkpatrick, J. D. 2005, ARA&A, 43, 195
Kluyver, T., Ragan-Kelley, B., Pérez, F., et al. 2016, ELPUB, 87
Lam, S. K., Pitrou, A., & Seibert, S. 2015, in Proc. of the Second Workshop on the LLVM Compiler Infrastructure in HPC. Numba: a LLVM-based Python JIT compiler, 7 (New York, NY, USA: ACM)
Lee, G., Helling, C., Dobbs-Dixon, I., & Juncher, D. 2015, A&A, 580, A12
Lewis, N. K., Showman, A. P., Fortney, J. J., Knutson, H. A., & Marley, M. S. 2014, ApJ, 795, 150
Lines, S., Mayne, N. J., Boutle, I. A., et al. 2018, A&A, 615, A97
Lines, S., Mayne, N. J., Manners, J., et al. 2019, MNRAS, 488, 1332
Livingston, J. H., Crossfield, I. J. M., Petigura, E. A., et al. 2018, AJ, 156, 277
Lodders, K. 2003, ApJ, 591, 1220
Lodders, K., & Fegley, B. 2002, Icar, 155, 393
MacDonald, R. J., Marley, M. S., Fortney, J. J., & Lewis, N. K. 2018, ApJ, 858, 69
Marley, M., & Robinson, T. 2015, ARA&A, 53, 279

Marley, M. S., Ackerman, A. S., Cuzzi, J. N., & Kitzmann, D. 2013, in Clouds and Hazes in Exoplanet Atmospheres, ed. S. J. Mackwell et al. (Tucson, AZ: Univ. Arizona Press), 367
Marley, M. S., Gelino, C., Stephens, D., Lunine, J. I., & Freedman, R. 1999, ApJ, 513, 879
Marley, M. S., Saumon, D., & Goldblatt, C. 2010, ApJL, 723, L117
McGouldrick, K., & Toon, O. B. 2007, Icar, 191, 1
McKinney, W. 2010, in Proc. of the 9th Python in Science Conf., Data Structures for Statistical Computing in Python, ed. S. van der Walt & J. Millman, 56
Morley, C. V., Fortney, J. J., Kempton, E. M.-R., et al. 2013, ApJ, 775, 33
Morley, C. V., Fortney, J. J., Marley, M. S., et al. 2012, ApJ, 756, 172
Morley, C. V., Fortney, J. J., Marley, M. S., et al. 2015, ApJ, 815, 110
Moses, J. I., Visscher, C., Fortney, J. J., et al. 2011, ApJ, 737, 15
Muñoz, A. G., & Isaak, K. G. 2015, PNAS, 112, 13461
Niraula, P., Redfield, S., de Wit, J., et al. 2018, arXiv:1812.09227
Oreshenko, M., Heng, K., & Demory, B.-O. 2016, MNRAS, 457, 3420
Parmentier, V., Fortney, J. J., Showman, A. P., Morley, C., & Marley, M. S. 2016, ApJ, 828, 22
Parmentier, V., Showman, A. P., & Fortney, J. J. 2021, MNRAS, 501, 78
Parmentier, V., Showman, A. P., & Lian, Y. 2013, A&A, 558, A91
Parviainen, H., Deeg, H. J., & Belmonte, J. A. 2013, A&A, 550, A67
Patzer, A., Chang, C., Sedlmayr, E., & Sulzle, D. 2005, EPJD, 32, 329
Pérez, F., & Granger, B. E. 2007, CSE, 9, 21
Powell, D., Louden, T., Kreidberg, L., et al. 2019, ApJ, 887, 170
Powell, D., Zhang, X., Gao, P., & Parmentier, V. 2018, ApJ, 860, 18
Pruppacher, H. R., & Klett, J. D. 1978, Homogeneous Nucleation (Dordrecht: Springer), 162
Roman, M., & Rauscher, E. 2019, ApJ, 872, 1
Roman, M., Kempton, E. M. R., Rauscher, E., et al. 2021, ApJ, 908, 101
Rowe, J., Matthews, J., Seager, S., et al. 2008, ApJ, 689, 1345
Samra, D., Helling, Ch., & Min, M. 2020, A&A, 639, A107
Saumon, D., & Marley, M. S. 2008, ApJ, 689, 1327
Seager, S., Whitney, B. A., & Sasselov, D. D. 2000, ApJ, 540, 504
Showman, A. P., Fortney, J. J., Lian, Y., et al. 2009, ApJ, 699, 564
Showman, A. P., & Kaspi, Y. 2013, ApJ, 776, 85
Showman, A. P., Lewis, N. K., & Fortney, J. J. 2015, ApJ, 801, 95
Showman, A. P., Tan, X., & Parmentier, V. 2020, SSRv, 216, 139
Shporer, A., & Hu, R. 2015, AJ, 150, 112
Sing, D., Fortney, J., Nikolov, N., et al. 2016, Natur, 529, 59
Skemer, A. J., Morley, C. V., Zimmerman, N. T., et al. 2016, ApJ, 817, 166
Smith, M. D. 1998, Icar, 132, 176
sqlite3 Development Team. 2019, DB-API 2.0 interface for SQLite databases. https://docs.python.org/3.4/library/sqlite3.html
Sudarsky, D., Burrows, A., & Hubeny, I. 2003, ApJ, 588, 1121
Toon, O., McKay, C., Griffith, C., & Turco, R. 1992, Icar, 95, 24
Visscher, C., Lodders, K., & Fegley, B. 2010, ApJ, 716, 1060
von Paris, P., Gratier, P., Borde, P., & Selsis, F. 2016, A&A, 587, A149
Walt, S., Colbert, V. D., Varoquaux, G., et al. 2011, CSE, 13, 22
Webber, M. W., Lewis, N. K., Marley, M., et al. 2015, ApJ, 804, 94
Wolf, E. T., & Toon, O. B. 2010, Sci, 328, 1266